# The Second LBA Calibrator Survey of southern compact extragalactic radio sources — LCS2

Leonid Petrov[1]⋆, Alet de Witt[2], Alessandra Bertarini[3], Elaine M. Sadler[4], Chris Phillips[5], and Shinji Horiuchi[6],

[1] *NASA, Goddard Space Flight Center, 8801 Greenbelt Rd, MD 22071, USA*
[2] *Hartebeesthoek Radio Astronomy Observatory, P.O.Box 443, Krugersdorp 1740, South Africa*
[3] *Institute of Geodesy and Geoinformation, University of Bonn, Nussallee 17, Bonn, Germany and*
*Max Planck Institute for Radioastronomy, Bonn, Germany*
[4] *Sydney Institute for Astronomy, School of Physics, The University of Sydney, NSW 2006, Australia*
[6] *CSIRO Astronomy and Space Science, PO Box 76, Epping, NSW 1710, Australia*
[7] *Shinji's affiliation, Australia*

**ABSTRACT**

We present the second catalogue of accurate positions and correlated flux densities for 1100 compact extragalactic radio sources that were not observed before 2008 at high resolution. The catalogue spans the declination range $[-90°, -30°]$ and was constructed from nineteen 24-hour VLBI observing sessions with the Australian Long Baseline Array at 8.3 GHz. The catalogue presents the final part of the program that was started in the 2008. The goals of that campaign are 1) to extend the number of compact radio sources with precise coordinates and measured correlated flux densities, which can be used for phase referencing observations, geodetic VLBI, search for sources with significant offset with respect to *Gaia* positions, and space navigation; 2) to extend the complete flux-limited sample of compact extragalactic sources to the southern hemisphere; and 3) to investigate the parsec-scale properties of sources from the high-frequency AT20G survey. The median uncertainty of the source positions is 3.5 mas. As a result of this VLBI campaign, the number of compact radio sources south of declination $-40°$ which have measured VLBI correlated flux densities and positions known to milliarcsecond accuracy has increased by a factor of 6.4. The catalogue and supporting material is available at `http://astrogeo.org/lcs`.

**Key words:** astrometry – catalogues – instrumentation: interferometers – radio continuum – surveys

## 1 INTRODUCTION

Until recently, the method of very long baseline interferometry (VLBI) proposed by Matveenko et al. (1965) was the only way to measure positions of extragalactic radio sources that are almost exclusively active galactic nuclea (AGNs) with sub-nanoradian accuracy. Recently, it has been demonstrated (Lindegren et al. 2016) that *Gaia* is able to get the position accuracy in par with VLBI. However, comparison of VLBI and *Gaia* matching sources showed (Mignard et al. 2016; Petrov & Kovalev 2017a) that there is a population of sources with statistically significant position offsets. A

more detailed analysis by Kovalev et al. (2017) revealed that VLBI/*Gaia* offsets have a preferred direction along the jet with the mean offset in a range of 1–2 mas that was interpreted as a manifestation of the contribution of optical jet to the centroid position. This allowed Petrov & Kovalev (2017b) to make a conclusion that VLBI/*Gaia* difference is due to the fact VLBI and *Gaia* see different part of a source and further improvement in accuracy beyond 1–2 mas level will not result in a reconciliation of VLBI and *Gaia* coordinates of active galaxies. Moreover, the VLBI/*Gaia* offsets brings an important signal that allows us to make an inference about milliarcsecond scale source structure of AGNs that currently cannot be observed directly. As a consequence, if we need achieve accuracy better 1–2 mas, we

⋆ E-mail:Leonid.Petrov@nasa.gov

cannot borrow *Gaia* positions of a matching sources, but have to rely on VLBI determination of source coordinates for applications that needs high accuracy, such as space navigation, Earth orientation parameter monitoring, and comparison of positions of pulsars determined with VLBI and timing.

In this context, it becomes increasingly important to have an all-sky, deep, and precise catalogue of positions of extragalactic sources from radio observations. The most productive instrument for absolute radio astrometry is the Very Long Baseline Array. Using VLBA, one can easily determine positions of sources at declinations [-30°, +90°] (Beasley et al. 2002; Petrov et al. 2005, 2006; Kovalev et al. 2007; Petrov et al. 2008; Petrov 2011, 2013; Petrov & Taylor 2011; Petrov et al. 2011a; Immer et al. 2011; Condon et al. 2017; Gordon et al. 2016; Petrov 2016); with some difficulties positions of sources at declinations [-45°, -30°] (Fomalont et al. 2003); but with some exceptions one cannot observe sources below -45°. The sequence of VLBA Calibrator Surveys 1–9 (VCS) (e.g., Petrov et al. 2008, and references therein) provided a dense grid of calibrator sources.

The lack of a VLBA analogue in the southern hemisphere resulted in the past in a significant hemisphere disparity of the source distribution in absolute radioastrometry catalogues. To alleviate this problem, we launched a program for observing radio sources at declinations [-90°, -40°] with Long Baseline Array (LBA) in 2008. The main goal of the program was to increase the density of calibrator sources with positions known at milliarcsecond level in the southern hemisphere to make an analogue of VCS in the south. Unlike to the VCS surveys at the northern hemisphere, we used predominately AT20G at 20 GHz from Australia Telescope Compact Array (ATCA) observations for drawing the candidate list for LBA observations.

The results of the first part of this campaign for observing the brightest sources, the catalogue LCS–1 was published by (Petrov et al. 2011b). Here we present results of the second, final part of the campaign. In the following sections we describe observations, data analysis, analysis of errors, and investigate the relationship of the correlated flux density at milliarcsecond scales derived from our VLBI observations with flux densities of the parent AT20G catalogues at arcsecond scales.

## 2    OBSERVATIONS

### 2.1    Network

The network of observing station includes 11 stations listed in Table 1, although at any given experiment only a subset of stations participated. The list of VLBI experiments, observation dates, and the participating network is shown in Table 2. The network, except station Hh, is shown in Figure 1. Station As participated in three experiments, station Td observed only during 4–8 hours intervals. The 64 m station PARKES was scheduled in every experiment, in every scan of target sources since it is the most sensitive station of the network and the baselines with Pa are the most sensitive.

Stations At, Mp and Cd were equipped with the LBA VLBI backend consisting of an Australia Telescope National Facility (ATNF) Data Acquisition System (DAS) with an

**Table 1.** The LBA network. The typical System Equivalent Flux Density (SEFD) at 8.3 GHz at elevation angles > 45° achieved in LCS experiments is shown in the last column.

| Code | Name | $\phi_{gc}$ | $\lambda$ | Diam | SEFD |
|------|------|-------------|-----------|------|------|
| As | ASKAP | -26°.53 | 116°.63 | 12 m | 8300 Jy |
| At | ATCA | -30°.15 | 149°.57 | 5 × 22 m | 140 Jy |
| Cd | CEDUNA | -31°.70 | 133°.81 | 32 m | 600 Jy |
| Ha | HARTRAO | -25°.74 | 27°.69 | 26 m | 1200 Jy |
| Ho | HOBART26 | -42°.62 | 147°.44 | 26 m | 850 Jy |
| Ke | KATH12M | -14°.28 | 132°.15 | 12 m | 3000 Jy |
| Mp | MOPRA | -31°.10 | 149°.10 | 22 m | 400 Jy |
| Pa | PARKES | -32°.82 | 148°.26 | 64 m | 50 Jy |
| Td | TIDBINBILLA | -35°.22 | 148°.98 | 34 m | 120 Jy |
| Yg | YARRA12M | -28°.88 | 115°.35 | 12 m | 3000 Jy |
| Ww | WARK12M | -36°.25 | 174°.66 | 12 m | 3000 Jy |
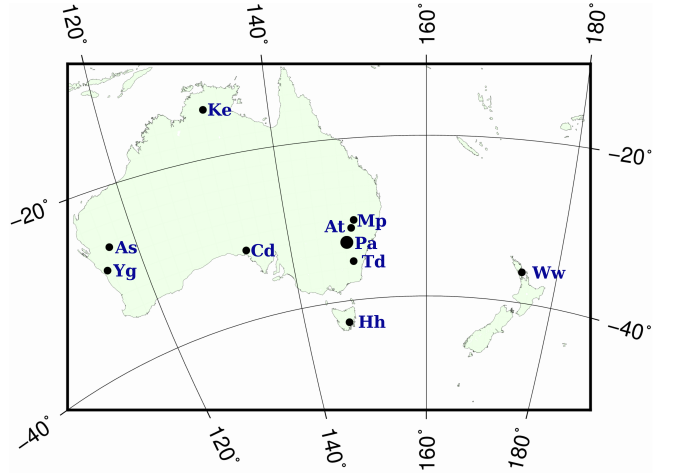


**Figure 1.** The LBA stations network. Station Hh (HARTRAO), 60 km north-west of Johannesburg, South Africa, is not shown.

LBADR recorder. The ATNF DAS only allows two simultaneous intermediate frequencies (IFs): either 2 frequencies or 2 polarizations. For each of these IFs the input 64 MHz analog IF is digitally filtered to 2 contiguous 16 MHz bands. Stations At and Mp were equipped with two LBDAR recorders, however additional recorders could not be used for expanding the bandwidth due to hardware limitations, but could be used for recording both polarizations. Thus, the stations equipped with the ATNF backend could record two bands 32 MHz wide. This imposed a limitation on the frequency setup: spreading the frequencies too narrow would result in degradation of group delay accuracy and spreading the frequencies two wide would results in group delay ambiguities with very narrow group delay ambiguities spacings. Our choice was to spread 32 MHz sub-bands at 256 MHz that allowed to determine group delay with uncertainly 123 ps when the signal to noise ratio is 10 and with ambiguity 3.9125 ns.

Other stations were equipped with Mark-4 data acquisition terminals that were replaced with Mark-5 during to the course of the campaign. Station Cd was upgraded from the ATNF backend to Mark-5 in 2015 and used Mark-5 in last three campaigns. Stations equipped with Mark-5 recorded

**Table 2.** List of the LBA Calibrator Survey experiments. The first column shows the campaign segment, the second and third show the observing session and experiment ID, and the last segment shows the network of participating stations.

| | | | |
|---|---|---|---|
| LCS–1 | 20080205_r | v254b | At-Cd-Ho-Mp-Pa |
| LCS–1 | 20080810_r | v271a | At-Cd-Ho-Mp-Pa-Td |
| LCS–1 | 20081128_r | v271b | At-Cd-Ho-Mp-Pa-Td |
| LCS–1 | 20090704_r | v271c | At-Cd-Ho-Mp-Pa |
| LCS–2 | 20091212_r | v271d | At-Cd-Ho-Mp-Pa |
| LCS–2 | 20100311_r | v271e | At-Cd-Ho-Mp-Pa |
| LCS–2 | 20100725_p | v271f | At-Cd-Ho-Mp-Pa |
| LCS–2 | 20101029_p | v271g | At-Cd-Mp-Pa |
| LCS–2 | 20110402_p | v271h | At-Cd-Ho-Hh-Ww-Td |
| LCS–2 | 20110723_p | v271i | As-At-Cd-Ho-Hh-Mp-Pa-Td-Ww |
| LCS–2 | 20111111_p | v271j | At-Cd-Ho-Hh-Mp-Td |
| LCS–2 | 20111112_p | v441a | At-Cd-Ho-Hh-Mp-Td |
| LCS–2 | 20120428_p | v271k | At-Cd-Ho-Hh-Mp-Pa-Ww-Yg |
| LCS–2 | 20130315_p | v271l | As-At-Cd-Ho-Hh-Mp-Pa-Ww-Td |
| LCS–2 | 20130615_p | v271m | At-Cd-Ho-Hh-Mp-Pa-Ww-Td |
| LCS–2 | 20140603_p | v493a | At-Cd-Ho-Hh-Mp-Pa-Td |
| LCS–2 | 20150407_p | v271n | At-Cd-Ho-Hh-Ke-Pa-Ww-Yg |
| LCS–2 | 20150929_q | v271o | As-At-Cd-Ho-Hh-Ke-Pa-Ww-Yg |
| LCS–2 | 20160628_q | v493c | As-At-Cd-Ke-Mp-Pa-Yg |
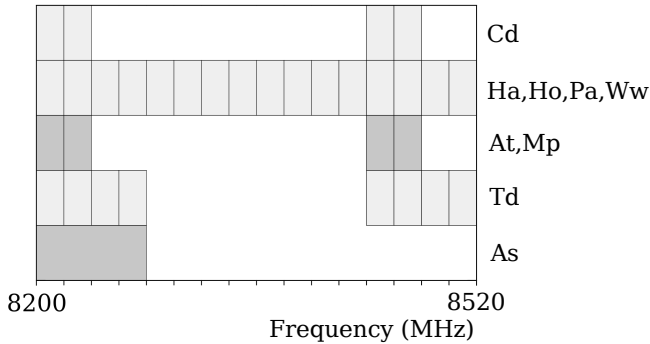
**Figure 2.** The frequency allocation in v271i experiment. The channel width is 16 MHz for all stations, except As, which has the channel width 64 MHz. Single polarization channels are shown with light-gray color and dual polarization channels are shown with dark-Gray color.

256 MHz bandwidth, except Td that prior 2016 was able to record only 128 MHz and station As that could record a single bandwidth 64 MHz, dual polarization. Stations equipped with Mark-4 or Mark-5 recorded more 16 MHz wide frequency channels with 320 MHz wide bandwidth that partly overlapped with the frequency channels recorded by the stations with the ATNF backend In every experiment network stations used from 2 to 5 different setups and these setups were changing from the experiment to experiment. Figure 2 shows as an example the frequency setup of v271i experiment. The versatility of the DiFX-2 correlator (Deller et al. 2011) allowed to cross-correlate the overlapping regions of such experiments. The heterogeneity of the the available VLBI hardware made correlation more difficult but, fortunately did not introduced noticeable systematic errors in group delay. The most profound effect of this frequency allocation is ambiguities in group delay at baselines with stations that record with the ATNF backend.
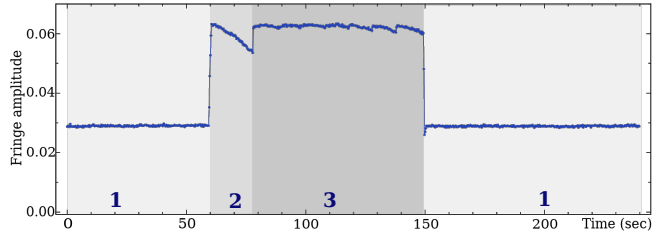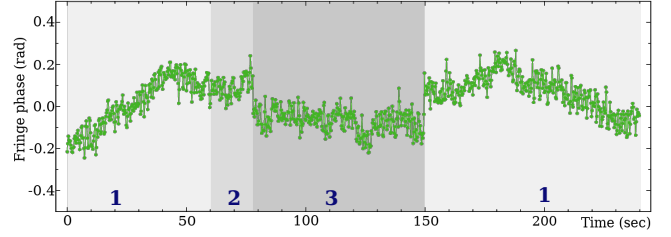
**Figure 3.** The fringe plot at ATCA/PARKES, source J2225-0457 during vt10k test experiment. The upper plot shows fringe phase, the lower plot shows fringe amplitude. Light-gray area "1" denotes the interval when single ATCA station records. The dark-gray area "3" denotes the interval when the phased-array records. The medium-gray area "2" denotes the intermediate interval.

The Australia Telescope Compact Array (ATCA) consists of six 22 m antennas. Five of them can be phased up and record signal as a single element of the VLBI network. The position of the ATCA phase center can be specified by the user. This feature became available in 2009 **Chris, correct?**. However, we exercised a caution in us- **Corr 1** ing phased ATCA since attempts to use phased Westerbork array for astrometry revealed significant phase fluctuations which rendered it highly problematic for precise astrometry (Pogrebenko, private communication, 2010). Therefore, we investigated performance of phase ATCA in a special 4 hour long test experiment that we ran on May 08, 2010. Stations ATCA, CEDUNA, HOBART26, MOPRA, and PARKES recorded the same frequency setup as in the LCS experiments. For the first 60 seconds of a 4 minute long scan ATCA recorded signal from the single antenna at pad with ID 104 (see LCS1 paper for the nomenclature of ATCA pads), then it switched to the phased array with the phase center at the same pad and recorded for 90 second. Finally, it ATCA switched back to recording the signal from a single station. In total, 232 scans of strong sources were recorded. The typical plots of the normalized uncalibrated fringe amplitude and fringe phase as a function of time within a scan are shown in figure 3.

We see that for 18 seconds after switching to the phased-up mode the fringe amplitude is steadily drops by 15% and then suddenly returns back and stays stable within 2%. We consider this as transitional interval. **Chris, we need to explain this behavior**. The fringe phase does not show **Corr 2** change greater 0.01 rad just after switching back to the phased mode, but shows a sudden change in a range of 0.1–0.2 rad after the end of the transitional interval and immediately after switching from the phased to the single antenna record mode.

We computed average fringe phases, phase delay rates, group delays and group delay rates by running the fringe fit-

ting algorithm trough the same data three times. During the first processing run we masked out single antenna recording mode and the first 18 s of the phased recording mode keeping 72 s long data in each scan when ATCA recorded in the phased mode. During the second processing run we masked out the data when ATCA recorded in the phased mode. During the third run we processed first 60 s and last 90 s of each scan when ATCA recorded in the single antenna mode. We referred group delay and fringe phases to the same common epoch within a scan and formed their differences.

The differences in group delay between phased and single antenna recording mode at different baselines with ATCA is shown on Figure 4 with green color. The weighted root mean square (wrms) of the differences is 38 ps. For comparison, the differences in group delays computed using the first 60 seconds and last 90 seconds of a 4 minute long scan recorded at ATCA in the single antenna mode and referred to the same middle epoch are shown with blue color. The wrms of these differences is 59 ps. The differences in fringe phase between recording at ATCA with phased model and single antenna mode are shown in Figure 5. The wrms of phase differences is 0.12 rad.

We analyzed dependence if the differences versus elevation, azimuth and parallactic angle, but found no pattern. The uncalibrated averaged fringe amplitude at baselines with ATCA data recorded as a phased array is a factor of 2.27 greater than the uncalibrated fringe amplitude with ATCA data recorded as a single antenna, which is within 2% of $\sqrt{5}$.

We conclude that phasing ATCA up does not introduce noticeable systematic errors in group delay and fringe phases. The differences in group delays is a factor of 1.5 less than the difference in group delay computed from two subset of data separated by 90 s. The differences in phases is random noise with wrms is 0.12 rad, which corresponds to 0.6 mm. Therefore, we concluded that using of phased ATCA as an element of the VLBI network does not introduce systematic errors, but improves sensitivity of ATCA by a factor of 2.27. This was the first use of phased array as an element of VLBI network for absolute astrometry.

## 2.2 Source selection

We selected for observations the target sources that were previously detected with single dish observations or with connected interferometers at baseline 0.1–5 km. The input catalogues provided the estimates of flux density at resolutions 1–100″. The response of an interferometer to an extended source depends on its compactness and the size of the interferometer. The baseline projection lengths of the LCS network vary in a range of 5–300 M$\lambda$. That means the interferometer will be sensitive for emission from the compact components of milliarcsecond size. The response to extended emission with a size more than 1 mas at the longest baselines and 50 mas at the shortest baselines will be attenuated, and the interferometer will not detect signal from emission with size a more than a factor 2–5 beyond that level.

In order to maximize the number of detected sources, we have to select the targets with the highest compactness: the ratio of the correlated flux density at 5–300 M$\lambda$ to the total flux density. As a marker of high compactness we initially used spectral index defined as $S \sim f^{\alpha}$, where $f$ is
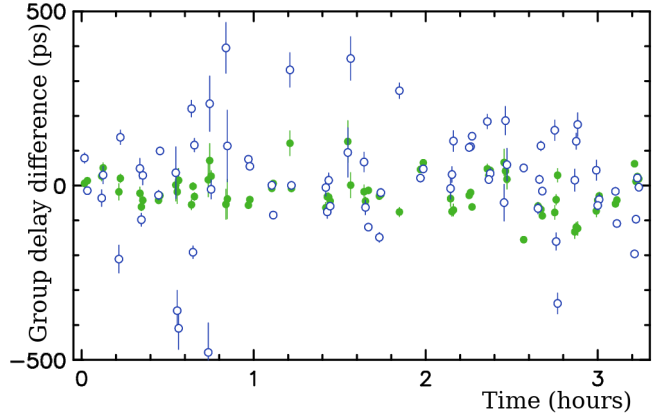


**Figure 4.** Differences in group delays from the same observations in test vt10k experiment. The solid green circles show the differences in group delay between ATCA phased-array and ATCA-single stations. The wrms of the differences is 38 ps. For comparison, the whole blue circles show the differences in group delay from first 60 sec and last 90 seconds of the integration interval.
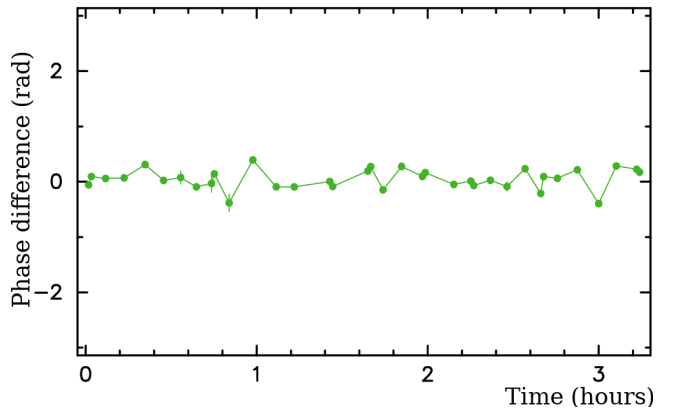


**Figure 5.** Differences in fringe phase delays between ATCA phased-array and ATCA-single recording from the same observations in test vt10k experiment. The wrms of the differences ins 0.12 rad.

the frequency. As a result of synchrotron self-absorption the emission from the optically thick jet based that is morphologically referred to as the core of an AGN, has flat ($\alpha \approx 0$) or inverted spectrum ($\alpha > 0$). The optically think emission from the extended jet and extended radio-lobes that are a result of interaction of the jet with surrounding interstellar medium usually has steep spectrum ($\alpha < 1$). Therefore, one can expect the sources with flat spectrum, on average, will have a higher compactness, which was confirmed with observations (e.g., Beasley et al. 2002).

For the coarse of the 8-year long campaign our sources selection strategy gradually evolved, but all the time it was focused on selecting the sources with brightest correlated flux density. In the first three experiments we selected the sources with spectral index $> -0.50$ from the quarter-Jansky survey (Jackson et al. 2002) brighter 200 mJy. In following experiments were used several criteria for selecting the targets. In experiments v271c–v271m we selected

the candidate sources brighter 150 mJy with spectral index $> -0.55$ from the AT20G catalogue (Murphy et al. 2010). In addition to that, we selected the sources brighter 180 mJy and spectral index $> -0.55$ from the PMN catalogue (Griffith & Wright 1993; Wright et al. 1994; Griffith et al. 1994; Condon et al. 1993; Tasker et al. 1994; Griffith et al. 1995; Wright et al. 1996). In v271k–v271m experiments we selected the sources brighter 170 mJy and spectral index $> -0.55$ from the ATPMN catalogue (McConnell et al. 2012).

However, an approach of selecting flat spectrum sources does not provide a good prediction for correlated flux density for the sources within 5–7° of the Galactic plane. First, the the Galactic plane is crowded and a chance to make an error in cross-matching the sources observed with instruments are different resolutions and poor positional accuracy rather high. This will result in a gross mistake in the estimate of the spectral indices. Second, the density of galactic sources with flat spectrum, such as supernova remnants and ultra-compact H II regions is much higher within the Galactic plane. An attempt to observe flat spectrum sources in the Galactic plane by cross-matching the MGPS-2 catalogue at 843 MHz Murphy et al. (2007) resulted in a detection rate of $\sim 10\%$. To overcome this problem, we used another approach to find candidate sources in the Galactic plane: we analyzed IR color-color diagram. Massaro et al. (2011) noticed that the blazars occupied a special zone in the color-color diagram 3.4–4.6 $\mu$m and 4.6–12 $\mu$m. We analyzed this dependence independently and delineated the zone that encompasses over 85% compact radio-loud AGNs from the cumulative VLBI catalogue RFC (Petrov & Kovalev, 2019, in preparation[1]). See section 4.2 in Schinzel et al. (2015) for detail. After the failure with cross matching MGPS-2 with higher frequency radio catalogues, we tried the second approach: we selected all the sources within 5° of the Galactic plane and declinations below $-40°$ and flux density $> 50$ mJy and left those that have cross-matches against IR WISE catalogue (Wright et al. 2010; Mainzer et al. 2011) within 30″. Then we throw away the sources that are away the zone of the 3.4–4.6 $\mu$m and 4.6–12 $\mu$m diagram that contains 85% radio loud AGNs. We observed the brightest sources from the remaining sample. The detection rate of this sample was 57%.

In addition to these selection methods, we observed in three experiments, v441a, v493a, and v493c the flat spectrum sources brighter 10 mJy that were detected at 5 and 9 GHz by the Australia Telescope Compact Array (ATCA) within its error ellipse, i.e. 2–5′ of unassociated sources $\gamma$-ray sources detected with *Fermi* mission (Abdo et al. 2010) that we found in a dedicated program (Petrov et al. 2013; Schinzel et al. 2015, 2017) focused in finding the most plausible radio counterparts of $\gamma$-ray source. Since radio-loud $\gamma$-ray AGNs tend to be very compact, the presence of a radio source detected with a connected interferometer within the error ellipse of a $\gamma$-ray raises the probability of being detected with VLBI. Observing such sources first, fits the primary goal of the LCS program, second, allows to find an association to *Fermi* objects that previously were considered unassociated.

[1] Preview is available at http://astrogeo.org/rfc

## 2.3 Scheduling

The experiment scheduled was generated automatically with program sur_sked in a sequence that minimizes the slewing time and obey a number of constraints. Target sources was observed in three-four scans for 2 to 4 minutes long each, except weak targets of candidates to *Fermi* associations that were observe for 5–10 minutes. Observing session had nominal duration of 24 hours. During a session 80–100 target sources were observed. The minimum gap between consecutive observations of the same source was set to 2.5 hours. Station PARKES was required to participate in each scan, since it is the most sensitive antenna of the array. After 1.5 hours of observing targets sources, a block of so-called calibrator sources was inserted. These are the sources picked from the pool of known compact objects stronger 300 mJy. The block consists of 4 sources, with two of them observed at each station in the elevations in the range of 10–30° (30–40° for PARKES that have elevation limit 31°) and two observed at elevations 55–85°. The goal of these observations: 1) to improve the estimate of the atmosphere path delay in zenith direction; 2) to connect the LCS catalogue to the accumulative catalogue of compact radio sources; 3) to use these sources as bandpass calibrator; 4) to use these sources as amplitude calibrators for elevation gain corrections.

## 3 DATA ANALYSIS

The antenna recorded voltage sampled with 2-bits and the aggregate bit rate from 256 to 1024 millions of samples per second. The first step of data analysis is correlation that is performed at the dedicated facility followed by post-correlator analysis that computes group delays and phase delay rates using the spectrum of cross-correlated data, followed by astrometric analysis that computes source positions, followed by amplitude analysis that either produces source images or estimates of the correlated flux density at the specified range of the lengths of projected baselines.

### 3.1 Correlation and post-correlation analysis

The first four experiments were correlated with the Bonn Mark4 Correlator. The data from ATCA-104, CEDUNA, and MOPRA, originally recorded in LBADR format were transformed to the Mark5B format before correlation. Correlation of the data from LBADR data acquisition rack against the data from the Mark-4 data acquisition terminal was complicated since this is a non-standard operation. Post-correlation analysis of these data was was performed at the correlator using software program FOURFIT, the baseline-based fringe fit offered within the Haystack Observatory Package Software (HOPS) to estimate the residual group delay and phase delay rate. More detail about processing these experiments can be found in Petrov et al. (2011b).

Other experiments were correlated with the DiFX software correlator (Deller et al. 2011) at the International Centre for Radio Astronomy Research, the joint venture between Curtin University and the University of Western Australia. The output of DiFX correlator was converted to FITS-IDI format and further processed with PIMA VLBI data analysis software Petrov et al. (2011a). The correlator provided

the time series of cross- auto-correlated output spectral resolution 0.25 MHz and time resolution 0.25 s. Such a choice of correlation parameters allowed to detect a sources within several arcminutes of pointing direction, i.e., everywhere within the primary beam of PARKES radio telescope that has full with half maximum (FWHM) at 8.4 GHz is $\sim 2'$.

The post-correlator analysis chain includes the following steps:

• Coarse fringe fitting that is performed using an abridged grid of group delays and delay rates without further refinement. The goals of this step is to find at each baseline 10–15 observations with the highest signal to noise ratio (SNR) and detect failures at one or more IFs

• Computation of complex bandpass using the 12 observations with the highest SNR. The complex bandpass describes a distortion of the phase and amplitude of the recorded signal with respect to the signal that reached the antennas. We flagged at this step the IFs that either were not recorded or failed. We used 12 observations for redundancy in order to evaluate the statistics of residual deviation of the phase and amplitude as a function of frequency from the ideal after applying the bandpass computed over 12 observations using least squares. Large residuals triggered detailed investigation that in a case of serious hardware problem resulted in flagging affected spectral channels.

• Fine fringe fitting that is performed using the complex bandpass and the bandpass mask derived in the previous step. The preliminary value of the group delay and phase delay is found as the maximum element of the two-dimensional Fourier transform of the time series of cross-correlation spectrum sampled over time and frequency with a step 4 times finer over each dimension than the data. The fine value of the group delay and phase delay rate is adjusted from phases of the cross-correlation function (also known as fringe phases) as small corrections to the preliminary values using least squares. Phase residuals of the cross-correlation spectrum are analyzed and additive corrections to the a priori weights are computed on the basis of this analysis. The uncertainties of estimates of group delays are derived from uncertainties of fringe phases and additive weights corrections. The uncertainties of fringe phases depend on fringe amplitudes. The explicit expression can be found on page 233 of Thompson et al. (2017).

• Computation of total group delays and phase delay rates. The group delays and phase delay rates computed at the previous step are corrections to the a priori delays and phase delay rates used during correlation. The mathematical model of the a priori group delay and phase rate used by the correlator is presented as a set of coefficients of polynomials at intervals of time that cover the time range of a VLBI experiment. Using these coefficients, the a priori group delays and phase delay rates are computed to a common epoch within a scan for the event of arriving the wavefront at a reference station of a baseline. Using these a priori group delays and phase delay rates, the total group delays for that epoch are formed.

### 3.2 Astrometric analysis

Group delay is the main observable for astrometric analysis. The a priori model of group delay, more sophisticated that
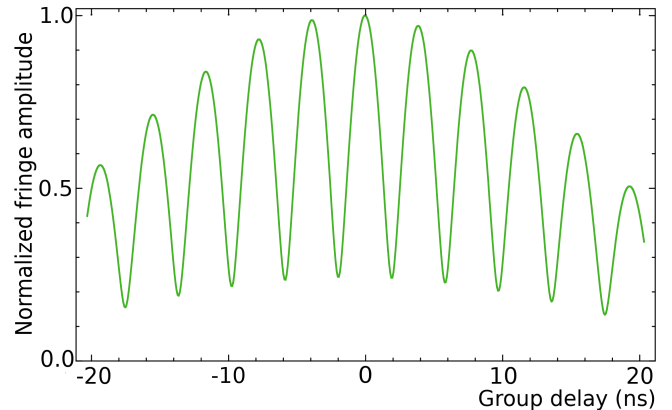


**Figure 6.** The normalized fringe amplitude as a function of group delay between stations that had LBDAR recording system. The fringe amplitude is divided by the amplitude at the global maximum.

that used for correlation is computed and the differences between observed and theoretical path delays are formed. The partial derivatives of this model over source coordinates, station positions, the Earth ordination parameters, atmosphere path delay in zenith direction, and clock function are computed corrections to that parameters are computed using least squares.

The frequency setup used for this campaign selected due to hardware limitation, see as an example the setup for v271i segment in Figure 2, posed a challenge in data analysis. The Fourier transform over frequency over baselines with At, Cd, Mp in this example that uses LBDAR data acquisition system has strong secondary maxima (see Figure 6). The amplitude of the 2nd maximum is 0.98, the third maximum 0.93, the fourth maximum 0.83 with respect of the global maximum. Due to the noise in data and phase distortion, the fringe fitting process cannot reliably distinguish the primary and the secondary maxima, and as a result, group delay is determined with the ambiguity of $N \times 1/2.56 \cdot 10^8 \approx 3.9$ ns, where $N$ is a random integer number, typically in a range [-2,2].

The first phase of astrometric data analysis is to clean for outliers in the so-called narrow-band group delays computed as an arithmetic average of group delays computed over each IF independently. The narrow-band delays do not have ambiguities, but are one order of magnitude less precise than group delays computed over the entire band. The estimated parameters at this stage are station positions and coordinates of target sources, as well as atmospheric path delays in zenith direction and clock function in a form of expansion over B-spline. The contribution of the adjusted parameters to path delay computed using the narrow-band delays is substituted to the group delay residuals and then used for initial resolving group delay ambiguities. The procedure for group delay ambiguity resolution is described in detail in Petrov et al. (2011b).

After the group delay ambiguities are resolved, the dataset is cleaned for outliers in group delay. If necessary, the parametric model of clock is refined for incorporating discontinuities at specified epochs. Initial data weights were chosen to be reciprocal to the group delay uncertainty $\sigma_g$.

Then the additive baseline-dependent wight corrections $a$ were computed for each observing session to make the ratio of the weighted sum of residuals be close to their mathematical expectation. These weights wee used in the initial solution. The weights in the final solution were used in the form

$$w = \frac{1}{k \cdot \sqrt{\sigma_g^2 + a^2 + b^2}}, \qquad (1)$$

where $k$ is a multiplicative factor and $b$ an additive weight correction for taking into account mismodeled ionosphere contribution to group delay (see below). Such clean dataset is used for further analysis.

The final LCS catalogue was derived using all dual-band X/S (8.4/2.3 GHz) observations since 1980 through July 2018 under geodesy and astrometry programs that are publicly available and 19 LCS X-band experiments in a single least square solution. The estimated parameters are split into three groups: global parameters that are estimated for the entire dataset, local parameters that are specific for a given experiment, and segmented parameters that are specific for a timer interval shorter than session duration. The global estimated parameters are coordinates of all observed sources, positions and velocities of all observing stations, harmonic variations of station positions at annual, semi-annual, diurnal, and semi-diurnal frequencies, B-spline coefficients that describe discontinuities and non-linear motion of station caused by seismic activity. The local parameters are pole coordinates UT1 and their first time derivative. The segmented parameters are clock function for all the station except the reference one, and residual atmosphere path delay in zenith direction.

For the course of LCS campaign, a number of target sources were observed in follow-up VLBI experiments. We excluded these sources from dual-band experiments in our LCS solution. The position of LCS target sources were derived using only LCS 8.4 GHz data. Observations of these sources were later used for evaluation of errors of the LCS catalogue and computation of the multiplicative weight correction $k$.

Since equations of electromagnetic wave propagation are invariant with respect to rotation of the celestial coordinate system, and translation and rotation of terrestrial coordinate system, the system of equations have a rank deficiency and determine only a family of solution. In order to define the solution from that family we applied no-net-rotation for source coordinates requiring the new catalogue of source position have no net-rotation for 212 so-called defining sources with respect to their positions in the ICRF1 catalogue (Ma et al. 1998). Similarly, we applied no-net-rotation and no-net-translation constraints on station positions.

### 3.3 Imaging analysis

**Alet and Alessandra: here is the place for your song.**

### 3.4 Determination of flux densities

**Here I will describe results of non-imaging analysis for those experiments Alet and Alessandra still did not process.**

## 4 ERROR ANALYSIS

Single-band group delays are affected by the contribution of the ionosphere Considering the ionosphere as a thin shell at a certain height above the Earth surface (typically 450 km), the group delay can be expressed as

$$\tau_{\text{iono}} = \frac{\alpha}{f_{\text{eff}}^2} \text{ TEC } \frac{1}{\cos \beta}, \qquad (2)$$

where $f_{\text{eff}}$ is the effective frequency, $\beta$ is the zenith angle at the ionosphere piercing point, TEC is the total electron contents in the zenith direction at the ionosphere piercing point, and $\alpha$ is a constant (see Sovers et al. (1998) for detail). We have computed the a priori ionosphere contribution to group path delay using TEC maps from analysis if Global Navigation Satellite System (GNSS) observations. Specifically, we used CODE TEC time series (Schaer 1999)[2] with resolution $5° \times 2.5° \times 1^h$ ($5° \times 2.5° \times 2^h$ before December 19, 2013).

The TEC model from GNSS observation is an approximation and the accuracy of a priori $\tau_{\text{iono}}$ from such a model is significantly lower than the accuracy of $\tau_{\text{iono}}$ computed from the linear combination of group delays at X and S (or X and C) bands from dual-band observations. The errors of $\tau_{\text{iono}}$ from latter observations is at level of several picoseconds according to Hawarey et al. (2005). We consider the contribution of mismodeled ionospheric path delay as dominating in the error budget and, therefore, we investigated it in detail.

We used the global dataset of VLBI observations after July 01, 1998 for investigation of the residual ionospheric contribution to group delay after applying the a priori path delay delay from CODE global TEC maps. For each dual-band observing sessions, we decompose the slant ionospheric path delay from X/S observations at the product of the path delay in zenith direction and the mapping function, the ratio of the ionospheric path delay in a given elevation to the the ionospheric path delay in zenith direction. Then we computed the rms of the total $\tau_{\text{iono}}$ in zenith direction from CODE global TEC maps and the rms of the residual $\tau_{\text{iono}}$ after subtracting the a priori ionospheric group delay in zenith direction computed from CODE global TEC maps from $\tau_{\text{iono}}$ in zenith direction derived from dual-band X/S group delays. The ratio of these two statistics, $A = \frac{\sigma_r^2}{\sigma_t^2}$ is a measure of a goodness of the model. Assuming $A$ is stable, we can predict unknown to us statistics of $\sigma_r^2$ for single-band observation using $\sigma_t^2$ that we can compute from TEC model. We computed the time series of parameter $A$.

Parameter $A$ is not stable with time. Since $A$ is computed as a ratio of variances, we sought an empirical regression models where $A$ enters as a multiplicative factor. We computed the global total electron content (GTEC),

---

[2] Available at ftp.aiub.unibe.ch/CODE/
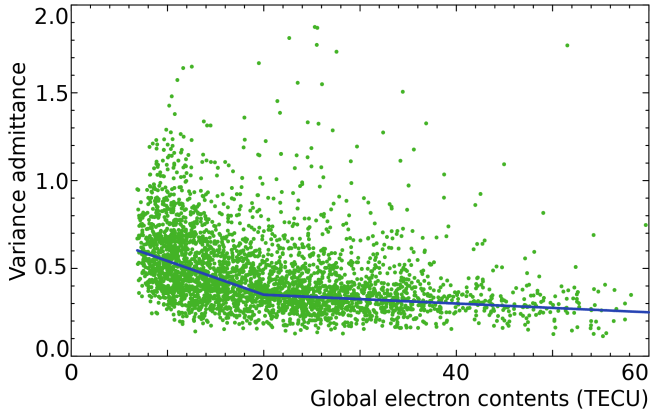
**Figure 7.** The dependence of the variance admittance factor $A$ on the global total electron contents. The so-called TEC units ($10^{16}$ electrons over zenith direction) are used for GTEC.



**Figure 8.** The distribution of the normalized arc lengths between LCS X-band only positions of 269 sources and their X/S positions from the follow-up campaigns (Green dots). For comparison, the Rayleigh distribution with $\sigma = 1$ parameter is shown with a blue line.

by averaging the TEC over the sphere. As it was show by Afraimovich et al. (2008), such a parameter characterizes the global state of the ionosphere. Figure refr:gtec shows the dependence of $A$ on GTEC. We represent this dependence with a broken linear function with A=0.6 at GTEC=7.0, A=0.35 at GTEC=20.0 and A=0.25 at GTEC=60.0.
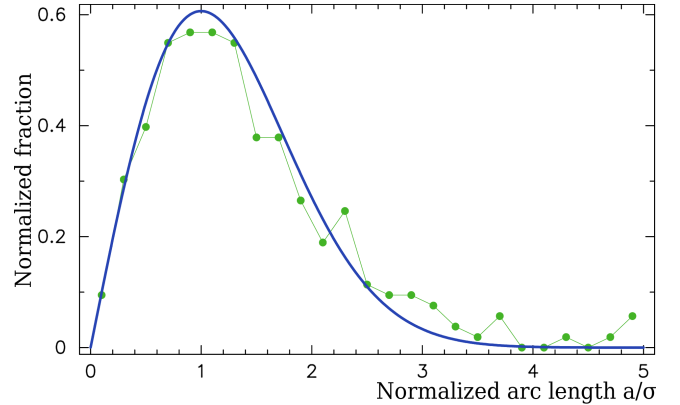
Using this dependence, for a given experiment we computed the GTEC, averaged it over the period of experiment duration, computed parameter $A$ using the liner regression, computed for each station of a baseline the time series of the ionospheric contribution from the GTEC model, and then computed the variances for the first and second station of a baseline, $Cov_{11}$ and $Cov_{22}$, as well as their covariances. Then for each observation we computed the predicted rms of mismodeled ionospheric contribution as

$$b = A\sqrt{Cov_{11}^2\, M_1^2(e) - 2\, Cov_{12}\, M_1(e)\, M_2(e) + Cov_{22}^2\, M_2^2(e)}, \quad (3)$$

where $M_1(e)$ and $M_2(e)$ are mapping function of the ionospheric path delay. These parameters $b$ were used for weight corrections in expression 1.

Parameter A varied from 0.35 to 0.59 with the mean 0.48 for the LCS campaign This means that applying the ionospheric contribution from the CODE TEC maps, we reduce the variance of the total contribution by a factor of 2, and the mismodeled part of the contribution is accounted in inflating uncertainty of group delay. The known deficiency of this approach is that first, the regression dependence of parameter on $A$ on GTEC is rather coarse, and second, the correlations between residual ionospheric contributions are neglected.

For a check of the contribution of remaining systematic errors, we compared our source positions derived from X-band only LCS experiments with results of dial-band observations that included some LCS target sources. In 2017, the SOuthern Astrometry Program (SOAP) of dual-band follow-up observations at stations Hh-Ho-Ke-Yg-Wa-Ww-Pa at 2.3/8.4 GHz commenced. The goal of the program is to improve positions of bright sources with declinations below $-45°$. Buy August 2018, 10 twenty-hour experiments were observed. In two of them, PARKES station participated. The sources as week as 70 mJy were observed in exper-

iments with PARKES, 2–3 scans per sources, and objects brighter 250 mJy were observed in other experiments, 8–10 scans per source. These experiments were made in the so-called geodetic frequency setup: 6 IFs of 16 MHz wide were spanned between 2.20 and 2.304 GHz (S-band) and 10 IFs of 16 MHz wide were spanned between 8.198 and 8.950 GHz (X-band). Group delays were computed for X and S band separately, and the ionosphere-free combinations group delays were formed. At the moment of writing, the program has not been completed, and a detailed analysis will be presented in the future upon completion of the program. Meanwhile, we use these 10 experiments to compare results and assess the errors.

We ran a reference global solution using all dual band X/S observations of the LCS target sources including the SOAP observations and excluding LCS observations. The reference and the LCS solutions differed in 1) the list of sessions that were used in the solutions and 2) in treatment of the atmosphere. The reference solution used ionosphere-free linear combinations of S and X-band observables, while the LCS solution used X-band only group delays, applied during data reduction the contribution to group delay caused by the ionosphere computed using the CODE TEC maps. The reference solution used weights according to expression 1 with k=1 and b=0.

We have compared the positions of 373 LCS target sources that are common with the reference solution. We did not find any outlier exceeding 20 mas that can be caused by errors in group delay ambiguity resolution. That means that all observations with unreliable ambiguity resolution were correctly flagged out and did not degrade the solution. At the same time, we found that the arc lengths divided by the their uncertainties, so-called normalized arcs, were larger than expected with the mean value 1.89. We attributed this discrepancy to underestimation of errors of LCS observations. To alleviate this underestimation we varied the multiplicative factor $k$ in expression 1 in such a way the distribution of normalized arcs be as close to the Rayleigh distribution with $\sigma = 1$ as possible. We found that when $k = 1.80$ is used for analysis of LCS observations, it approximates the
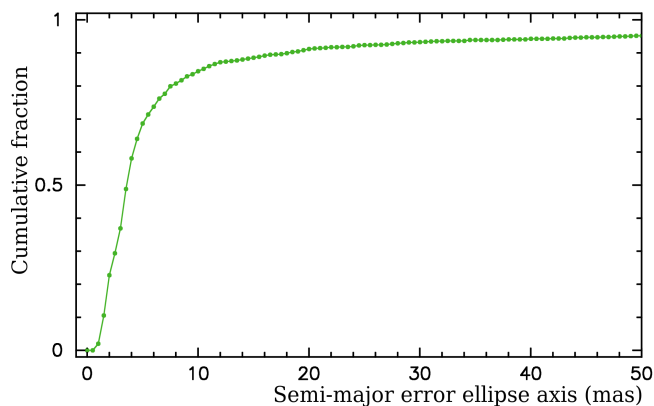
**Figure 9.** The cumulative distribution of the LCS position errors.

distribution of normalized arcs over 269 sources that have at least 16 observations the Rayleigh distribution the best way. The mean arc length is 3.4 mas and the median value is 2.5 mas. The cumulative distribution of the final LCS position errors is shown in Figure 9.

## 5  THE CATALOGUE

The first 8 rows of the LCS catalogue are presented in Table 3 The catalogue presents source positions, position uncertainties, the number of used observations, flux densities in three ranges of baseline projection lengths, and their formal uncertainties. In total, the catalogue has 1100 entries. The median semi-major error ellipse axes of reported positions is 3.6 mas. The flux densities are in a range from 3 mJy to 2.5 Jy, with the median 102 mJy. For completeness, the list of 405 sources that have been observed, but not observed is given in the machine-readable table.

The distribution of LCS sources on the sky is shown in Figure 10. The distribution is rather uniform and does not have avoidance zones. For comparison, the sources known priori the LCS campaign are shown with blue color.

## 6  DISCUSSION

The median position uncertainty, 3.6 mas, cannot be called the VLBI state of the art nowadays. There are four factors that played the role. First, the contribution of the ionosphere cannot be computed using GNSS TEC models with the same level of accuracy as using simultaneous dual-band observations. Second, the scale of the network, less 1700 km for the most observations degraded the sensitivity of observations to source positions, since source position uncertainty is reciprocal to the baseline length. Station HARTRAO participated ion less than 25% observations. Third, the spanned bandwidth was limited to 320 MHz, compare with 720 MHz typically used in geodetic VLBI. Position uncertainty is approximately reciprocal to the spanned bandwidth. Fourth, observed sources were rather week: 25% target sources are weaker 46 mJy.

Nevertheless, position accuracy of several milliarcseconds is sufficient for phase referencing. Figure 11 shows the probability to find a phase calibrator brighter 30 mJy within
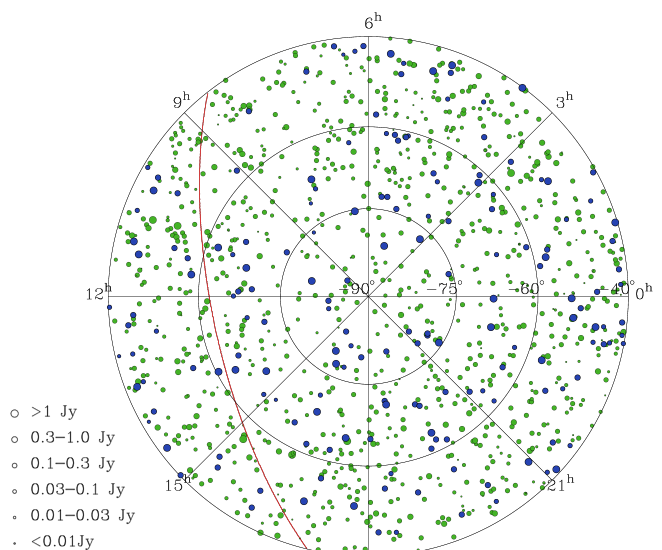
**Figure 10.** The sky distribution of compact radio sources at the southern hemisphere. Blue light color denotes 186 sources with declinations $< -40°$ with VLBI positions known prior the LCS program. Green dark color denotes 1100 sources detected in LCS program. Red line shows the Galactic plane.

$2°$ of any target with $\delta < -40°$. For 88% of the area, such a calibrator can be found.

Among 1100 LCS sources, there are 725 counterparts with Gaia DR2 (Kovalev et al. 2017) with the probability of false detection above 0.0002. See Petrov & Kovalev (2017a) for detail of the VLBI and Gaia association procedure. Petrov et al. (2018) showed that comparison of over 9,000 matched VLBI/Gaia sources reveled that 9% have statistically significant offsets at the level exceeding $4\sigma$. They present extensive argumentation that these offsets are real and are the manifestation of the presence of optical jets that affect positions of optic centroid reported by Gaia. The LCS dataset has 53 (7.2%) outliers with arc length exceeding $4\sigma$. The lower fraction of outliers is explained by worse position accuracy. These outliers were excluded from further analysis, since they do not characterize errors of the catalogues. The median arc length of position differences is 3.2 mas, while the median semi-major error ellipse axes of LCS positions of matched sources is 3.3 mas and the median semi-major error ellipse of Gaia positions of matched sources is 0.3 mas. This comparison demonstrates that the median position differences between LCS and Gaia positions is very close to the reported median of LCS semi-major error axis.

For analysis of LCS completeness we computed the so-called logN–logS diagram — the dependence of the the logarithm of number of sources on the logarithm of the total flux density recovered from VLBI observations. The dependence is approximated with a straight line within that range of flux densities the catalogue is considered complete. With a decrease of flux density, at some point the diagram deviates from the straight line. That point is considered the limit of below which the catalogue is incomplete. The diagram in Figure 12 shows the completeness level of LCS at $\delta < -40°$ is 120 mJy is over 95%.
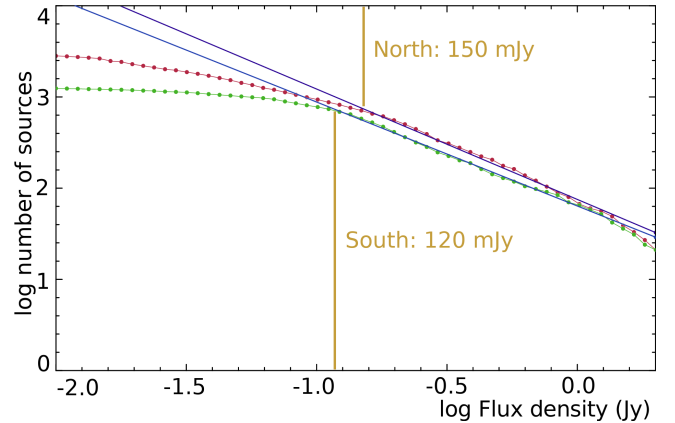
For comparison we computed similar diagram at north-

| (1) | (2) | (3)<br>hh mm ss.fffff | (4)<br>° ′ ″ | (5)<br>mas | (6)<br>mas | (7) | (8) | (9)<br>Jy | (10)<br>Jy | (11)<br>Jy | (12)<br>Jy | (13)<br>Jy | (14)<br>Jy |
|---|---|---|---|---|---|---|---|---|---|---|---|---|---|
| LCS J0001−4155 | 2358−422 | 00 01 32.75494 | −41 55 25.3367 | 215.1 | 92.3 | -0.904 | 5 | 0.008 | 0.007 | -1.0 | 0.001 | 0.002 | -1.0 |
| LCS J0002−6726 | 2359−677 | 00 02 15.19280 | −67 26 53.4337 | 89.6 | 32.8 | 0.553 | 5 | 0.006 | 0.007 | -1.0 | 0.001 | 0.001 | -1.0 |
| LCS J0002−5621 | 0000−566 | 00 02 53.46830 | −56 21 10.7831 | 23.8 | 9.3 | 0.421 | 8 | 0.172 | 0.052 | 0.141 | 0.013 | 0.012 | 0.031 |
| LCS J0003−5444 | 0000−550 | 00 03 10.63084 | −54 44 55.9923 | 42.1 | 10.7 | -0.112 | 9 | 0.006 | 0.006 | -1.0 | 0.001 | 0.001 | -1.0 |
| LCS J0003−5247 | 0000−530 | 00 03 19.60042 | −52 47 27.2834 | 39.0 | 18.5 | -0.291 | 8 | 0.013 | 0.014 | -1.0 | 0.002 | 0.002 | -1.0 |
| LCS J0004−4345 | 0001−440 | 00 04 07.25762 | −43 45 10.1469 | 4.0 | 3.0 | 0.163 | 44 | 0.188 | 0.205 | 0.214 | 0.030 | 0.024 | 0.046 |
| LCS J0004−5254 | 0001−531 | 00 04 14.01314 | −52 54 58.7099 | 8.8 | 3.7 | 0.039 | 36 | 0.027 | 0.027 | 0.018 | 0.002 | 0.003 | 0.003 |

**Table 3.** The first 8 rows of the LCS catalogue. Columns: (1) source ID; (2) alternative source name; (3) J2000 right ascension; (4) J2000 declination; (5) uncertainty in right ascension without $\cos \delta$ factor; (6) uncertainty in declination; (7) correlation between right ascension and declination estimates; (8) the number of observations used in the solution; (9) the median correlated flux density at baseline projection lengths in a range 0–10 M$\lambda$; (10) the median correlated flux density at baseline projection lengths in a range 10–40 M$\lambda$; (11) the median correlated flux density at baseline projection lengths in a range 40–300 M$\lambda$; 12) the median uncertainty of the correlated flux density at baseline projection lengths in a range 0–10 M$\lambda$; (13) the median uncertainty of the correlated flux density at baseline projection lengths in a range 10–40 M$\lambda$; (14) the median uncertainty of the correlated flux density at baseline projection lengths in a range 40–300 M$\lambda$. This table is available in its entirety in machine-readable and Virtual Observatory (VO) forms in the online journal. A portion is shown here for guidance regarding its form and content.
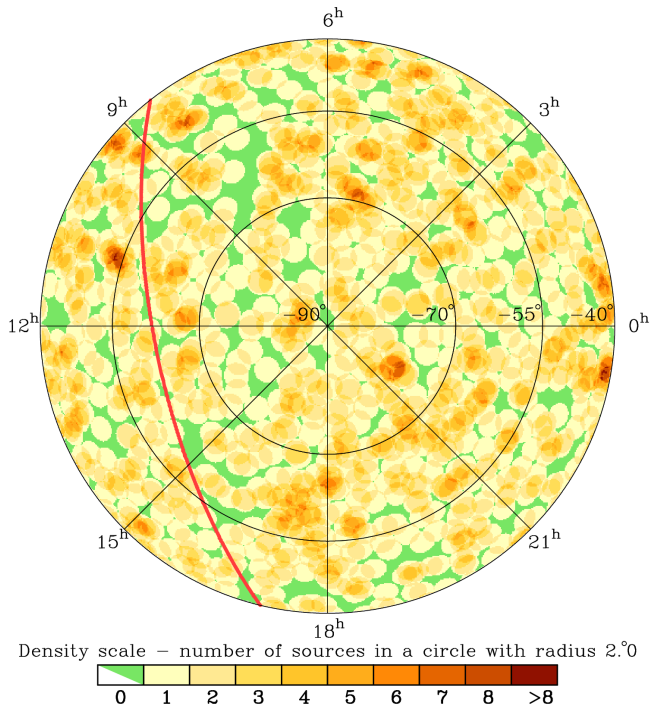


**Figure 11.** The sky density of calibrator sources in the zone with declinations $< -40°$ defined as the number of compact sources with flux density $> 30$ mJy in a circle of $2°$ radius. The Galactic plane is shown with the red line.



**Figure 12.** The log N–log S diagram for the LCS catalogue (low green line) using only the sources with $\delta < -40°$. The upper red line shows similar diagram for the sources with $\delta > +40°$.

sult in omitting the objects with falling spectrum. The logN–logS dependencies for southern and northern hemisphere are almost parallel in a range of 0.15–0.65 Jy. If we accept the hypothesis that selecting candidate sources based on AT20G causes a bias, we have to admit that using AT20G as a parent sample we lose sources as bright as 0.5 Jy, which is somewhat unexpected. More observations are need in order to resolve the problem.

## 7    SUMMARY

The LCS VLBI observing program provided positions of 1100 compact radio sources at declinations below $-30°$ known with accuracies at a milliarcsecond level and estimates of their flux density at 8.3 GHz. As a result, the number of compact radio sources south of declination $-40°$ which have measured VLBI correlated flux densities and positions known to milliarcsecond accuracy has increased by a factor of 6.4. The internal LCS is at 95% at a level of 120 mJy based on logN–logS diagram. At the same time, comparing LCS with the northern hemisphere catalogue we found a $\sim 20\%$ difference in the source count. The LCS may

ern hemisphere VLBI catalogue at declinations $> +40°$. The northern hemisphere catalogue has more weak sources, but surprisingly, its completeness at 95% is 150 mJy. At the same time, the northern hemisphere catalogue has 23% more sources. One explanation is the total number of sources in the southern hemisphere is indeed $\sim 20$scale fluctuation of the source distribution over the sky. Another explanation is a selection bias. The parent catalogue of the LCS is a AT20G at 20 GHz, while the parent catalogues of the northern hemisphere sources were observed at lower frequencies: 5–8 GHz. Selecting sources based in their emission at 20 GHz may re-

have a deficiency of ∼20% sources because of using AT20G as a parent sample. It is yet to be resolved whether using high-frequency sample catalogue results in systematic loss of sources with falling spectrum. The LCS catalogue is the southern hemisphere counterpart of VLBI Calibrator Survey. The major outcome if this campaign is elimination of the hemisphere bias that the VLBI catalogues suffered in the past. However, technical limitations of the southern hemisphere telescopes provided accuracy one order of magnitude worse than the accuracy of similar catalogues in the northern hemisphere. Future observations will be targeted to improving positions of LCS sources, and the first such follow-up observing campaign started in 2017.

## ACKNOWLEDGMENTS

## REFERENCES

Abdo A. A., et al., 2010, ApJS, 188, 405
Afraimovich E. L., Astafyeva E. I., Oinats A. V., Yasukevich Y. V., Zhivetiev I. V., 2008, Annales Geophysicae, 26, 335
Beasley A. J., Gordon D., Peck A. B., Petrov L., MacMillan D. S., Fomalont E. B., Ma C., 2002, ApJS, 141, 13
Condon J. J., Griffith M. R., Wright A. E., 1993, AJ, 106, 1095
Condon J. J., Darling J., Kovalev Y. Y., Petrov L., 2017, ApJ, 834, 184
Deller A. T., et al., 2011, PASP, 123, 275
Fomalont E. B., Petrov L., MacMillan D. S., Gordon D., Ma C., 2003, AJ, 126, 2562
Gordon D., et al., 2016, AJ, 151, 154
Griffith M. R., Wright A. E., 1993, AJ, 105, 1666
Griffith M. R., Wright A. E., Burke B. F., Ekers R. D., 1994, ApJS, 90, 179
Griffith M. R., Wright A. E., Burke B. F., Ekers R. D., 1995, ApJS, 97, 347
Hawarey M., Hobiger T., Schuh H., 2005, Geophys. Res. Lett., 32, L11304
Immer K., et al., 2011, ApJS, 194, 25
Jackson C. A., Wall J. V., Shaver P. A., Kellermann K. I., Hook I. M., Hawkins M. R. S., 2002, A&A, 386, 97
Kovalev Y. Y., Petrov L., Fomalont E. B., Gordon D., 2007, AJ, 133, 1236
Kovalev Y. Y., Petrov L., Plavin A. V., 2017, A&A, 598, L1
Lindegren L., et al., 2016, A&A, 595, A4
Ma C., et al., 1998, AJ, 116, 516
Mainzer A., et al., 2011, ApJ, 731, 53
Massaro F., D'Abrusco R., Ajello M., Grindlay J. E., Smith H. A., 2011, ApJ, 740, L48
Matveenko L. I., Kardashev N.-S., Sholomitskii G.-B., 1965, Soviet Radiophys., 461, 461
McConnell D., Sadler E. M., Murphy T., Ekers R. D., 2012, MNRAS, 422, 1527
Mignard F., et al., 2016, A&A, 595, A5
Murphy T., Mauch T., Green A., Hunstead R. W., Piestrzynska B., Kels A. P., Sztajer P., 2007, MNRAS, 382, 382
Murphy T., et al., 2010, MNRAS, 402, 2403
Petrov L., 2011, AJ, 142, 105
Petrov L., 2013, AJ, 146, 5
Petrov L., 2016, preprint, (arXiv:1610.04951)

Petrov L., Kovalev Y. Y., 2017a, MNRAS, 467, L71
Petrov L., Kovalev Y. Y., 2017b, MNRAS, 471, 3775
Petrov L., Taylor G. B., 2011, AJ, 142, 89
Petrov L., Kovalev Y. Y., Fomalont E. B., Gordon D., 2005, AJ, 129, 1163
Petrov L., Kovalev Y. Y., Fomalont E. B., Gordon D., 2006, AJ, 131, 1872
Petrov L., Kovalev Y. Y., Fomalont E. B., Gordon D., 2008, AJ, 136, 580
Petrov L., Kovalev Y. Y., Fomalont E. B., Gordon D., 2011a, AJ, 142, 35
Petrov L., Phillips C., Bertarini A., Murphy T., Sadler E. M., 2011b, MNRAS, 414, 2528
Petrov L., Mahony E. K., Edwards P. G., Sadler E. M., Schinzel F. K., McConnell D., 2013, MNRAS, 432, 1294
Petrov L., Kovalev Y. Y., Plavin A. V., 2018, preprint, (arXiv:1808.05114)
Schaer S., 1999, Geod.-Geophys. Arb. Schweiz, Vol. 59,, 59
Schinzel F. K., Petrov L., Taylor G. B., Mahony E. K., Edwards P. G., Kovalev Y. Y., 2015, ApJS, 217, 4
Schinzel F. K., Petrov L., Taylor G. B., Edwards P. G., 2017, ApJ, 838, 139
Sovers O. J., Fanselow J. L., Jacobs C. S., 1998, Reviews of Modern Physics, 70, 1393
Tasker N. J., Condon J. J., Wright A. E., Griffith M. R., 1994, AJ, 107, 2115
Thompson A. R., Moran J. M., Swenson Jr. G. W., 2017, Interferometry and Synthesis in Radio Astronomy, 3rd Edition. Springer, doi:10.1007/978-3-319-44431-4
Wright A. E., Griffith M. R., Burke B. F., Ekers R. D., 1994, ApJS, 91, 111
Wright A. E., Griffith M. R., Hunt A. J., Troup E., Burke B. F., Ekers R. D., 1996, ApJS, 103, 145
Wright E. L., et al., 2010, AJ, 140, 1868